Mesoscale particle-based simulations of flow in expansion–contraction microchannels at low Reynolds number

by

Clara Maria De La Torre Garcia

A thesis submitted to the Graduate Faculty of
Auburn University
in partial fulfillment of the
requirements for the Degree of
Master of Science

Auburn, Alabama
August 9, 2025

Keywords: dissipative particle dynamics, Stokes flow, enhanced oil recovery

Approved by

Michael P. Howard, Chair, Assistant Professor of Chemical Engineering
Panagiotis Mistriotis, Assistant Professor of Chemical Engineering
Symone Alexander, Assistant Professor of Chemical Engineering

Abstract

Polymer flooding is an enhanced oil recovery technique that enables the extraction of significantly more oil than conventional methods. The good performance of polymer flooding is believed to stem from a phenomenon known as elastic turbulence, a hydrodynamic instability that can occur for low Reynolds number flows through expansion–contraction microchannels. Experiments have shown that oil recovery efficiency is influenced by the polymer's architecture and hydrophobic associations. However, it remains unclear whether these changes are linked to elastic turbulence because little is known about how a polymer's molecular structure impacts this phenomenon. Mesoscale particle-based simulations are a promising approach to address this knowledge gap; however, they have not yet been applied to elastic turbulence. As a first step toward doing so, we have simulated the low-Reynolds-number flow of a Newtonian fluid through an expansion–contraction microchannel. The validity of the simulations was assessed using a theoretical solution derived using a regular perturbation method. The simulations were in good agreement with theory for microchannel geometries in which the theory was expected to be accurate, but the simulations also enabled us to simulate flows for which the theory was not accurate. This work establishes a baseline against which simulations with different polymers can be compared to characterize the presence of elastic turbulence.

Acknowledgments

I would like to express my sincere gratitude to my advisor, Dr. Michael Howard, for his guidance, support, and encouragement throughout the course of my research and academic journey. His mentorship has been instrumental in shaping both my academic and professional development.

I am also sincerely thankful to the department of Chemical Engineering at Auburn University for being a home to me for the past two years. The Chemical Engineering department at Auburn University fosters a collaborative and intellectually stimulating environment which has allowed me to grow both as academically and as a person. I also wanted to extend my appreciation to the faculty and staff of the Chemical Engineering Department at Auburn University for everything they have done for me and all their support and guidance.

Special thanks to my lab mates and fellow graduate students for their friendship, time, and help through my stay here at Auburn University. I am also grateful to the funding agencies and institutional support that made this research possible.

Finally, I would like to thank my family and friends for their love, patience, dedication and encouragement. I wouldn't have been able to make it without you. Their belief in me has been invaluable.

Table of Contents

List of Figures

Chapter 1

Introduction

Petroleum products derived from refining crude oil are essential to every day life as they are used to propel vehicles, heat buildings, produce electricity, and serve as feedstock to commodity chemicals.[1,2] The United States has been the world's leading oil producer since 2018, averaging approximately 13.2 million barrels of oil per day in 2024.[3] During the same year, crude oil contributed 27% of the nation's total energy production.[3] In 2020, oil supplied roughly one-third of the total energy consumed in the United States, with transportation accounting for the largest share of that usage.[4] These statistics highlight the importance of effective oil recovery technologies to meet the world's energy demands even while other sources of energy are developed and adopted.

Oil production may include up to three phases of recovery.[5] During primary recovery, oil is extracted using energy derived from the expansion of reservoir fluids, release of solution gas as pressure declines, aquifer support, and gravity drainage, typically yielding only 5–15% of the original oil in place (OOIP).[6–8] Secondary recovery, also known as pressure maintenance, follows with the injection of fluids (typically water or gas) to restore pressure and displace additional oil.[6,7] Waterflooding, the most common secondary method, mobilizes oil through viscous displacement, though it is often limited by viscous fingering, a phenomena where low-viscosity water channels through the more viscous oil and reduces recovery efficiency.[7] Secondary methods can usually recover an additional 10–25% of the OOIP, bringing the total recovery to 20–40% of the OOIP.[5] Tertiary recovery, or enhanced oil recovery (EOR), is performed when secondary methods become ineffective. EOR involves the injection of substances

not naturally present in the reservoir such as chemicals, gases, or heat to improve oil mobilization and extend field productivity.[6] EOR techniques can recover an additional 5–20% to bring the total recovery to 30–60% of the OOIP, depending on the reservoir characteristics and the method used.[5]

EOR can be divided into four categories: miscible, chemical, thermal, and microbial flooding processes.[7] Miscible flooding processes involve the injection of a gas that is miscible with the oil at the pressure and temperature of the reservoir.[6] Chemical flooding involves injecting fluids containing additives such as polymers, micellar polymers, and alkaline solutions to improve sweep efficiency or reduce the interfacial tension between the injected fluid and the oil.[7] Thermal flooding processes involve raising the temperature of the reservoir by injecting a hot fluid or by combusting the oil to decrease the oil viscosity.[7] Microbial flooding involves injecting microorganisms, assisting in the production of residual oil by reacting with the reservoir fluids.[7]

Polymer flooding (PF) is an economic, widely implemented chemical flooding process.[9,10] PF uses solutions of high-molecular-weight polymers to displace oil trapped in reservoirs by increasing the viscosity of the displacing fluid.[11] PF is considered highly effective, with ultimate oil recovery factors often reaching 50% of the OOIP.[9] Effective design and evaluation of PF processes requires a thorough understanding of how reservoir conditions influence polymer rheology, thermal stability, and adsorption onto rock surfaces.[12] The important rheological properties for EOR[9] are typically complex viscosity (related to resistance to flow[13]) and elastic modulus (related to deformation[14]). Thermal stability is a critical property for polymers used in EOR. The polymers must remain effective over extended periods under reservoir conditions, but at elevated temperatures, polymers are prone to thermal degradation. Additionally, in high-salinity reservoir brines, they may precipitate or undergo conformational changes that further reduce their performance.[12] Excessive polymer adsorption onto reservoir rocks diminishes flood efficiency, making low adsorption rates crucial for cost-effective recovery.[12] Other selection criteria for polymers includes compatibility with reservoir brine, chemical biological and shear stability, injectivity, and cost.[12]

Partially hydrolyzed polyacrylamide (HPAM) and xanthan gum (XG) are common polymers for PF, each offering distinct advantages and limitations depending on reservoir conditions.[9] HPAM, a commercially available copolymer of acrylamide and acrylic acid (or its salts), is the most widely used polymer for PF in industry.[9] HPAM offers effective viscosification under low-temperature and low-salinity conditions.[9,15] It is favored in field applications due to its excellent water solubility, viscosifying capability, favorable rheological properties, mobility control efficiency, and overall cost effectiveness.[9,15] XG is a high molecular weight natural polysaccharide typically produced by the fermentation process of a bacterium called *Xanthomonas*.[9] Although XG offers superior resistance to shear and mechanical degradation compared to PAM-based copolymers, it is less widely used due to its higher cost, susceptibility to biodegradation, injectivity challenges, and viscosity loss caused by biochemical reactions.[9,16] Additionally, it is not suitable for reservoirs with temperatures above 93°C, where thermal stability becomes a limiting factor.[9] In the United States, the temperatures of some reservoirs range from 60°C to 120°C, which means some surpass the thermal limit of XG.[17] On the other hand, reservoir temperatures commonly reach 100°C in the Middle East, well above the thermal degradation limit.[18] The overall recovery efficiency of OOIP for PAM copolymers was found to be 53% and the overall recovery efficiency of XG was found to be 45%.[19]

When a polymer solution is injected during PF, it displaces the resident fluids, oil, and water by flowing through expanding and contracting pore spaces.[11] The polymers must respond to spatial confinement, velocity gradients, and geometric transitions, all of which may contribute significantly to the resulting sweep efficiency and displacement performance in the field.[20–23] These flows are characterized by small Reynolds numbers where viscous forces dominate and laminar behavior is typically expected. However, it has been observed that elastic polymers flowing in such geometries can undergo a surprising flow instability known as elastic turbulence.[24–26] This phenomenon arises as polymer molecules stretch under deformation, generating elastic stresses that impart memory to the fluid and trigger chaotic flow patterns even in the absence of inertia.[25] Elastic turbulence is marked by a significant increase in flow resistance, the emergence of a wide range of spatial and temporal flow scales, a steeper power-law decay in the velocity power spectrum, and a substantial transfer of energy spanning several orders

of magnitude within the inertial-scale range.[25] In the context of PF and EOR, such elastic instabilities may enhance mixing and displacement efficiency well beyond what is predicted by classical viscous flow theories, offering a compelling explanation for the improved performance observed in PF.[27–30]

Elastic turbulence may depend on the architecture and chemistry of the polymers involved because recovery efficiency during PF has been observed to depend on these properties.[15,31–34] For example, star-like hydrophobically associative polyacrylamide (SHPAM), consisting of a nano-silica core with a shell of amphiphilic polymer chains that can hydrophobically associate,[34] exhibited markedly improved thickening performance, increased long-term stability, and enhanced viscoelastic properties, making it a more effective viscosifier under challenging reservoir conditions.[34] It is particularly striking that SHPAM outperforms HPAM considering that a bulkier polymer like SHPAM would typically be expected to exhibit poorer performance due to the increased likelihood of pore plugging.[15,31,34] The specific polymer characteristics responsible for improving performance in PF remain poorly understood, highlighting the need for further investigation into this fundamental knowledge gap.

Traditional analytical approaches or continuum-based computational fluid dynamics (CFD) methods typically use highly idealized polymer models that are unfortunately not well-suited for studying the influence of molecular-level features on elastic turbulence.[35,36] In contrast, mesoscale particle-based simulation methods can directly model polymer structure and interactions,[37] potentially offering critical insight into the underlying mechanisms driving elastic turbulence. However, mesoscale particle-based simulations have not yet been applied to study elastic turbulence.

To make progress toward this problem, we have simulated the laminar flow of a Newtonian fluid through an expansion–contraction microchannel, a geometry that is expected to produce elastic turbulence for a polymer solution,[38] using the dissipative particle dynamics (DPD) method. DPD was used because it enables the simulation of larger systems over longer timescales than traditional molecular dynamics, and it is well-suited for both polymers and multiphase flows.[39] Our long-term goal is to rationally engineer better polymers for flooding

processes, and the results from these simulations serve as a baseline for future simulations aiming to model elastic turbulence.

The rest of this thesis is organized as follows. First, we define the microchannel geometry being simulated and extend a theoretical solution for the flow in this geometry based on a regular perturbation method.[40] Second, we describe the DPD simulations performed in the same microchannel. Third, we compare our simulations to the theoretical solution in varying microchannel geometries. We demonstrate overall good agreement in regimes where the theoretical solution is expected to be accurate, but the DPD simulations allow us to study flows in channels for which the theoretical solution becomes inaccurate. Last, we conclude with some forward looking remarks on how extensions of our DPD simulations may be used to study elastic turbulence.

Chapter 2

Theory

The expansion–contraction microchannel being considered is effectively two dimensional (Figure 2.1), with a net flow in the x direction, boundary walls in the y direction, and no flow in the z direction. The half width between the walls H varies with x according to

$$H(x) = \frac{W}{2} + A\cos\left(\frac{2\pi x}{L}\right), \tag{2.1}$$

where L is the microchannel length, W is the average distance between the walls, and A is an amplitude. The distance between the microchannel walls at the expansion and contraction points is hence $W \pm 2A$. The microchannel nominally also has width D in the z direction, and there are periodic boundary conditions in x and z. As a result, the fluid lies in $-L/2 \leq x < L/2$, $-H(x) \leq y \leq H(x)$, and $-D/2 \leq z < D/2$.

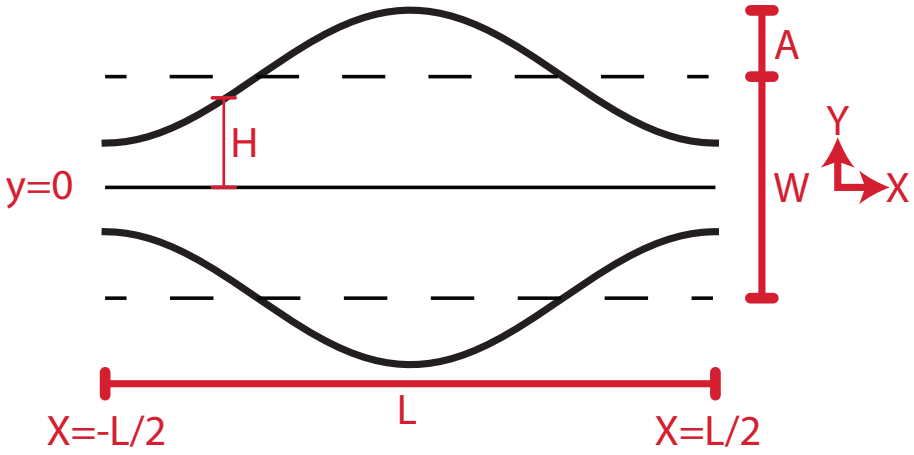

Figure 2.1: Sinusoidal expansion–contraction microchannel.

Kitanidis and Dykaar studied the flow of a Newtonian fluid in a similar geometry at low Reynolds numbers and obtained a fourth-order series solution.[40] Their approach is based on a stream function formulation of the Stokes equations, which they solved using a regular perturbation method with small parameter $\epsilon = W/L$. This solution is expected to be reasonably accurate when the channel is sufficiently long compared to the average wall separation, but they did not test its range of validity. Their derivation also has some notational inconsistencies and missing details. Hence, here, we outline how the stream function formulation and regular perturbation method can be used to solve for the flow in this microchannel. We also extend the solution to higher order for reasons that will be discussed in Chapter 4.

2.1 Problem formulation

Assuming a steady incompressible flow of a Newtonian fluid at low Reynolds number, the velocity field $\mathbf{u}$ is governed by the Stokes equations[41]

$$\nabla \cdot \mathbf{u} = 0 \tag{2.2}$$

$$\nabla \cdot \boldsymbol{\sigma} = \mathbf{0}, \tag{2.3}$$

where $\boldsymbol{\sigma} = -p\boldsymbol{\delta} + \boldsymbol{\tau}$ is the stress tensor, p is the pressure, $\boldsymbol{\delta}$ is the identity tensor, and $\boldsymbol{\tau}$ is the deviatoric stress tensor. (Written this way, the pressure may also include a conservative force acting on the fluid.) For an incompressible Newtonian fluid, $\boldsymbol{\tau} = \mu[\nabla\mathbf{u} + (\nabla\mathbf{u})^{\mathrm{T}}]$ so Eq. (2.3) is equivalent to

$$\mu\nabla^2\mathbf{u} = \nabla p. \tag{2.4}$$

The boundary conditions are no slip or penetration at the walls so $\mathbf{u} = \mathbf{0}$ at $y = \pm H$; periodicity in x so $\mathbf{u}$ is equal at $x = \pm L/2$; and a constant pressure drop $\Delta p > 0$ between $x = -L/2$ and $x = L/2$ that drives the flow in the positive x direction. By symmetry, there should be no flow in the z direction so $u_z = 0$ everywhere, and $\mathbf{u}$ should not depend on z.

For such two-dimensional planar flows, the Stokes equations can be reformulated using a stream function $\psi(x, y)$. The velocity field will satisfy the continuity equation Eq. (2.2) if

$$u_x = \frac{\partial \psi}{\partial y}, \quad u_y = -\frac{\partial \psi}{\partial x} \tag{2.5}$$

or equivalently,

$$\mathbf{u} = \nabla \times (\psi \mathbf{e}_z), \tag{2.6}$$

where $\mathbf{e}_z$ is the basis function in the z direction. Additionally, note that taking the curl of Eq. (2.4) gives

$$\nabla^2(\nabla \times \mathbf{u}) = \mathbf{0} \tag{2.7}$$

and that

$$\nabla \times \mathbf{u} = \nabla \times [\nabla \times (\psi \mathbf{e}_z)] = -\nabla^2(\psi \mathbf{e}_z) \tag{2.8}$$

because ψ does not depend on z. Hence, the stream function must satisfy the biharmonic equation

$$\nabla^4 \psi = \frac{\partial^4 \psi}{\partial x^4} + 2\frac{\partial^4 \psi}{\partial x^2 \partial y^2} + \frac{\partial^4 \psi}{\partial y^4} = 0. \tag{2.9}$$

The boundary conditions on the velocity become boundary conditions on the corresponding first derivatives of ψ at the boundaries.

Following Kitadanis and Dyakaar,[40] we reformulate the pressure boundary condition as an auxiliary condition on the volumetric flow rate Q by balancing the rate of work done on the fluid[42] with the rate of viscous dissipation $\mu\Phi$,

$$\int_{S_c} \mathbf{n} \cdot \boldsymbol{\sigma} \cdot \mathbf{u} \mathrm{d}\mathbf{x} = \int_{V_c} \mu \Phi \mathrm{d}\mathbf{x}, \tag{2.10}$$

where S_c is the closed boundary surface of the microchannel V_c with outer normal $\mathbf{n}$. The local rate of viscous dissipation is[42]

$$\mu\Phi = \boldsymbol{\tau} : \nabla\mathbf{u} = 2\mu\left[\left(\frac{\partial u_x}{\partial x}\right)^2 + \frac{1}{2}\left(\frac{\partial u_y}{\partial x} + \frac{\partial u_x}{\partial y}\right)^2 + \left(\frac{\partial u_y}{\partial y}\right)^2\right]. \tag{2.11}$$

We expect $\boldsymbol{\tau}$ to be periodic because it is a function of $\mathbf{u}$, which along with the boundary conditions and the integral definition of the volumetric flow through a surface S,

$$Q = \int_S \mathbf{n}\cdot\mathbf{u}\mathrm{d}\mathbf{x}, \tag{2.12}$$

allows the first integral to be evaluated as ΔpQ. Substituting the stream function gives

$$\Delta pQ = \mu\int_{V_\mathrm{c}}\left[4\left(\frac{\partial^2\psi}{\partial x\partial y}\right)^2 + \left(\frac{\partial^2\psi}{\partial y^2} - \frac{\partial^2\psi}{\partial x^2}\right)^2\right]\mathrm{d}\mathbf{x}. \tag{2.13}$$

We further note that Q is related to the stream function by Stokes' theorem,

$$Q = \int_S \mathbf{n}\cdot[\nabla\times(\psi\mathbf{e}_z)]\mathrm{d}\mathbf{x} = \oint_C(\psi\mathbf{e}_z)\cdot\mathrm{d}\mathbf{x} = [\psi(x,H) - \psi(x,-H)]D \tag{2.14}$$

where C is the boundary curve of S. The stream function is only defined up to a constant so we can arbitrarily choose $\psi(x,-H) = -Q/(2D)$, then this condition implies $\psi(x,H) = Q/(2D)$.

2.2 Nondimensionalization

Again following Kitadanis and Dyakaar,[40] we now nondimensionalize the equations. Lengths are made dimensionless by W. The stream function is made dimensionless by $WU_\parallel$, where

$$U_\parallel = \frac{W^2}{12\mu}\frac{\Delta p}{L} \tag{2.15}$$

is the average velocity in a parallel-plate microchannel ($A = 0$). The volumetric flow rate is also made dimensionless by that of the parallel-plate microchannel, $Q_\parallel = WDU_\parallel$. All dimensionless quantities in this chapter will be denoted by a hat. The biharmonic equation

becomes

$$\frac{\partial^4\hat{\psi}}{\partial\hat{x}^4} + 2\frac{\partial^4\hat{\psi}}{\partial\hat{x}^2\partial\hat{y}^2} + \frac{\partial^4\hat{\psi}}{\partial\hat{y}^4} = 0. \tag{2.16}$$

Additionally, the half-width of the channel becomes

$$\hat{H} = \frac{1}{2} + \hat{A}\cos(2\pi\epsilon\hat{x}) \tag{2.17}$$

where $\epsilon = W/L$, so $-\hat{L}/2 \leq \hat{x} < \hat{L}/2$ and $-\hat{H}(\hat{x}) \leq \hat{y} \leq \hat{H}(\hat{x})$. The auxiliary conditions become

$$\hat{Q} = \frac{\epsilon}{12}\int_{-\hat{L}/2}^{\hat{L}/2}\int_{-\hat{H}}^{\hat{H}}\hat{\Phi}\mathrm{d}\hat{y}\mathrm{d}\hat{x} \tag{2.18}$$

with

$$\hat{\Phi} = 4\left(\frac{\partial^2\hat{\psi}}{\partial\hat{x}\partial\hat{y}}\right)^2 + \left(\frac{\partial^2\hat{\psi}}{\partial\hat{y}^2} - \frac{\partial^2\hat{\psi}}{\partial\hat{x}^2}\right)^2 \tag{2.19}$$

and $\hat{\psi}(\hat{x}, \pm\hat{H}) = \pm\hat{Q}/2$. The remaining boundary conditions on the first derivatives of $\hat{\psi}$ transform straightforwardly.

2.3 Solution

An analytical solution to the biharmonic equation [Eq. (2.16)] with these boundary conditions is not known, but an approximate solution can be derived using a regular perturbation method with small parameter ϵ,[40] i.e., microchannels that are long compared to their average width. To apply this technique, we define rescaled coordinates $\eta = \epsilon\hat{x}$ and $\xi = \hat{y}/\hat{H}$, which are bounded $-1/2 \leq \eta < 1/2$ and $-1 \leq \xi \leq 1$.[40] The half width of the channel becomes a function of only η

$$\hat{H} = \frac{1}{2} + \hat{A}\cos(2\pi\eta), \tag{2.20}$$

while the auxiliary conditions become

$$\hat{Q} = \frac{1}{12}\int_{-1/2}^{1/2}\int_{-1}^{1}\hat{\Phi}\hat{H}d\xi d\eta \tag{2.21}$$

and $\hat{\psi}(\eta, \pm 1) = \pm\hat{Q}/2$.

Some care must be taken in transforming the derivatives of $\hat{\psi}$. For example,

$$\frac{\partial \hat{\psi}}{\partial \hat{x}} = \epsilon \left(\frac{\partial \hat{\psi}}{\partial \eta} - \xi \frac{\hat{H}_1}{\hat{H}} \frac{\partial \hat{\psi}}{\partial \xi} \right) \tag{2.22}$$

$$\frac{\partial \hat{\psi}}{\partial \hat{y}} = \frac{1}{\hat{H}} \frac{\partial \hat{\psi}}{\partial \xi}, \tag{2.23}$$

where $\hat{H}_i$ designates the i-th derivative of $\hat{H}$ with respect η. Fortuitously, these derivatives transform the boundary conditions to similar forms, $\partial\hat{\psi}/\partial\xi = 0$ and $\partial\hat{\psi}/\partial\eta = 0$ at $\xi = \pm 1$ and $\partial\hat{\psi}/\partial\xi$ and $\partial\hat{\psi}/\partial\eta$ equal at $\eta = \pm 1/2$. This process must be repeated for higher-order derivatives to transform Eq. (2.16), which is tedious by hand.

Using the regular perturbation method, we sought solutions of the form

$$\hat{\psi}(\eta, \xi) = \sum_{n=0}^{N} \hat{\psi}_n(\eta, \xi) \epsilon^n, \tag{2.24}$$

where $\{\psi_n\}$ are unknown functions to be determined. Given the form of the auxiliary condition Eq. (2.21), we expect

$$\hat{Q} = \sum_{n=0}^{N} \hat{Q}_n \epsilon^n \tag{2.25}$$

to have a corresponding series, where $\hat{Q}_n$ are also unknown coefficients to be determined. The series for $\hat{\psi}$ can be substituted in the transformed biharmonic equation, then like-powers of ϵ are collected to obtain a set of partial differential equations for $\{\hat{\psi}_n\}$. These partial differential equations can be solved using only the boundary conditions $\partial\hat{\psi}_n/\partial\xi = 0$ at $\xi = \pm 1$ and $\hat{\psi}_n = \pm\hat{Q}_n/2$ at $\xi = \pm 1$. The solutions for $\{\hat{\psi}_n\}$ contain the unknown coefficients $\{\hat{Q}_n\}$, but they can be determined by substituting $\{\hat{\psi}_n\}$ in Eq. (2.21) and solving a linear system of equations for $\{\hat{Q}_n\}$. We performed these calculations using Mathematica version 14.2.1.0, which enabled us to expand on prior work[40] and obtain a tenth-order ($N = 10$) series solution. The series solution contained only even powers of ϵ, so we present only the key results for these terms after setting odd-power terms to zero.

2.3.1 Zeroth-order solution

The partial differential equation for $n = 0$ was

$$\partial_{0,4}\hat{\psi}_0 = 0, \tag{2.26}$$

where $\partial_{i,j}\hat{\psi}$ is the i-th partial derivative with respect to η and j-th partial derivative with respect to ξ of $\hat{\psi}$. The solution for $\hat{\psi}_0$ was

$$\hat{\psi}_0 = \hat{f}_0\hat{Q}_0 \tag{2.27}$$

with

$$\hat{f}_0 = -\frac{1}{4}\xi\left(\xi^2 - 3\right). \tag{2.28}$$

The corresponding solution for $\hat{Q}_0$ was

$$\hat{Q}_0 = \frac{1}{\hat{I}_0} \tag{2.29}$$

with

$$\hat{I}_0 = \frac{1}{8}\int_{-1/2}^{1/2} \hat{H}^{-3}\mathrm{d}\eta. \tag{2.30}$$

2.3.2 Second-order solution

The partial differential equation for $n = 2$ was

$$\begin{aligned}\partial_{0,4}\hat{\psi}_2 + 2\hat{H}_1^2\left[6\partial_{0,2}\hat{\psi}_0 + \xi\left(6\partial_{0,3}\hat{\psi}_0 + \xi\,\partial_{0,4}\hat{\psi}_0\right)\right] + 2\hat{H}^2\partial_{2,2}\hat{\psi}_0 \\ = 2\hat{H}\left[\hat{H}_2\left(2\partial_{0,2}\hat{\psi}_0 + \xi\,\partial_{0,3}\hat{\psi}_0\right) + 2\hat{H}_1\left(2\partial_{1,2}\hat{\psi}_0 + \xi\,\partial_{1,3}\hat{\psi}_0\right)\right],\end{aligned} \tag{2.31}$$

and the solution for $\hat{\psi}_2$ was

$$\hat{\psi}_2 = \hat{f}_2\hat{Q}_0 + \hat{f}_0\hat{Q}_2 \tag{2.32}$$

with

$$\hat{f}_2 = \frac{3}{40}\xi\left(\xi^2 - 1\right)^2\left(4\hat{H}_1^2 - \hat{H}\hat{H}_2\right). \tag{2.33}$$

The corresponding solution for $\hat{Q}_2$ was

$$\hat{Q}_2 = \frac{\hat{I}_2}{\hat{I}_0^2} \tag{2.34}$$

with

$$\hat{I}_2 = \frac{1}{20}\int_{-1/2}^{1/2} \left(\hat{H}\hat{H}_2 - 5\hat{H}_1^2\right)\hat{H}^{-3}\mathrm{d}\eta. \tag{2.35}$$

2.3.3 Fourth-order solution

The partial differential equation for $n = 4$ was

$$\begin{aligned}
&\partial_{0,4}\hat{\psi}_4 + \hat{H}^2\Big[2\partial_{2,2}\hat{\psi}_2 + 3\xi\hat{H}_2^2\Big(2\partial_{0,1}\hat{\psi}_0 + \xi\,\partial_{0,2}\hat{\psi}_0\Big)\Big] \\
&\quad + \xi\hat{H}_1^4\Big[\xi\Big(\xi^2\partial_{0,4}\hat{\psi}_0 + 12\xi\partial_{0,3}\hat{\psi}_0 + 36\partial_{0,2}\hat{\psi}_0\Big) + 24\partial_{0,1}\hat{\psi}_0\Big] \\
&\quad + 2\hat{H}_1^2\Big[\xi^2\partial_{0,4}\hat{\psi}_2 + 6\xi\partial_{0,3}\hat{\psi}_2 + 6\partial_{0,2}\hat{\psi}_2 \\
&\qquad - 3\xi\hat{H}\hat{H}_2\Big(\xi^2\partial_{0,3}\hat{\psi}_0 + 6\xi\partial_{0,2}\hat{\psi}_0 + 6\partial_{0,1}\hat{\psi}_0\Big) \\
&\qquad + 3\xi\hat{H}^2\Big(2\partial_{2,1}\hat{\psi}_0 + \xi\,\partial_{2,2}\hat{\psi}_0\Big)\Big] \\
&\quad + 4\hat{H}\hat{H}_1\Big(- 2\partial_{1,2}\hat{\psi}_2 - \xi\,\partial_{1,3}\hat{\psi}_2 \\
&\qquad + \xi\hat{H}\Big[\hat{H}_3\Big(2\partial_{0,1}\hat{\psi}_0 + \xi\,\partial_{0,2}\hat{\psi}_0\Big) + 3\hat{H}_2\Big(2\partial_{1,1}\hat{\psi}_0 + \xi\,\partial_{1,2}\hat{\psi}_0\Big)\Big] \\
&\qquad - \xi\hat{H}^2\partial_{3,1}\hat{\psi}_0\Big) \\
&\quad + \hat{H}^4\partial_{4,0}\hat{\psi}_0 \\
&\quad = \hat{H}\Big[2\hat{H}_2\Big(2\partial_{0,2}\hat{\psi}_2 + \xi\,\partial_{0,3}\hat{\psi}_2\Big) \\
&\qquad + 4\xi\hat{H}_1^3\Big(\xi^2\partial_{1,3}\hat{\psi}_0 + 6\xi\partial_{1,2}\hat{\psi}_0 + 6\partial_{1,1}\hat{\psi}_0\Big) \\
&\qquad + \xi\hat{H}^2\Big(\hat{H}_4\partial_{0,1}\hat{\psi}_0 + 4\hat{H}_3\partial_{1,1}\hat{\psi}_0 + 6\hat{H}_2\partial_{2,1}\hat{\psi}_0\Big)\Big],
\end{aligned} \tag{2.36}$$

and the solution for $\hat{\psi}_4$ was

$$\hat{\psi}_4 = \hat{f}_4\hat{Q}_0 + \hat{f}_2\hat{Q}_2 + \hat{f}_0\hat{Q}_4 \tag{2.37}$$

with

$$\begin{aligned}\hat{f}_4 = &-\frac{1}{5600}\xi\left(\xi^2-1\right)^2\Big[24\left(75\xi^2+17\right)\hat{H}_1^4\\&+\hat{H}^2\Big[\left(19-15\xi^2\right)\hat{H}\hat{H}_4+90\left(2\xi^2-3\right)\hat{H}_2^2\Big]\\&+8\left(30\xi^2-31\right)\hat{H}^2\hat{H}_3\hat{H}_1-36\left(50\xi^2-19\right)\hat{H}\hat{H}_1^2\hat{H}_2\Big].\end{aligned} \tag{2.38}$$

The corresponding solution for $\hat{Q}_4$ was

$$\hat{Q}_4 = \frac{\hat{I}_2^2-\hat{I}_0\hat{I}_4}{\hat{I}_0^3} \tag{2.39}$$

with

$$\begin{aligned}\hat{I}_4 = \frac{1}{1400}\int_{-1/2}^{1/2}\big(&-4\hat{H}^3\hat{H}_4+54\hat{H}^2\hat{H}_2^2+87\hat{H}_1^4\\&+56\hat{H}^2\hat{H}_3\hat{H}_1-306\hat{H}\hat{H}_1^2\hat{H}_2\big)\hat{H}^{-3}\mathrm{d}\eta.\end{aligned} \tag{2.40}$$

2.3.4 Sixth-order solution

The partial differential equation for $n = 6$ was

$$\begin{aligned}&\partial_{0,4}\hat{\psi}_6+\hat{H}^2\Big[2\partial_{2,2}\hat{\psi}_4+3\xi\hat{H}_2^2\Big(2\partial_{0,1}\hat{\psi}_2+\xi\,\partial_{0,2}\hat{\psi}_2\Big)\Big]\\&\quad+\xi\hat{H}_1^4\Big[\xi\Big(\xi^2\partial_{0,4}\hat{\psi}_2+12\xi\partial_{0,3}\hat{\psi}_2+36\partial_{0,2}\hat{\psi}_2\Big)+24\partial_{0,1}\hat{\psi}_2\Big]\\&\quad+2\hat{H}_1^2\Big[\xi^2\partial_{0,4}\hat{\psi}_4+6\xi\partial_{0,3}\hat{\psi}_4+6\partial_{0,2}\hat{\psi}_4\\&\qquad-3\xi\hat{H}\hat{H}_2\Big(\xi^2\partial_{0,3}\hat{\psi}_2+6\xi\partial_{0,2}\hat{\psi}_2+6\partial_{0,1}\hat{\psi}_2\Big)\\&\qquad+3\xi\hat{H}^2\Big(2\partial_{2,1}\hat{\psi}_2+\xi\,\partial_{2,2}\hat{\psi}_2\Big)\Big]\\&\quad+4\hat{H}\hat{H}_1\Big(-2\partial_{1,2}\hat{\psi}_4-\xi\partial_{1,3}\hat{\psi}_4\\&\qquad+\xi\hat{H}\Big[\hat{H}_3\Big(2\partial_{0,1}\hat{\psi}_2+\xi\partial_{0,2}\hat{\psi}_2\Big)+3\hat{H}_2\Big(2\partial_{1,1}\hat{\psi}_2+\xi\partial_{1,2}\hat{\psi}_2\Big)\Big]\\&\qquad-\xi\hat{H}^2\partial_{3,1}\hat{\psi}_2\Big)\end{aligned}$$

$$
\begin{aligned}
&+ \hat{H}^4 \partial_{4,0} \hat{\psi}_2 \\
&= \hat{H} \Big[2\hat{H}_2 \Big(2\partial_{0,2}\hat{\psi}_4 + \xi \partial_{0,3}\hat{\psi}_4 \Big) \\
&\quad + 4\xi \hat{H}_1^3 \Big(\xi^2 \partial_{1,3}\hat{\psi}_2 + 6\xi \partial_{1,2}\hat{\psi}_2 + 6\partial_{1,1}\hat{\psi}_2 \Big) \\
&\quad + \xi \hat{H}^2 \Big(\hat{H}_4 \partial_{0,1}\hat{\psi}_2 + 4\hat{H}_3 \partial_{1,1}\hat{\psi}_2 + 6\hat{H}_2 \partial_{2,1}\hat{\psi}_2 \Big) \Big],
\end{aligned} \tag{2.41}
$$

and the solution for $\hat{\psi}_6$ was

$$
\hat{\psi}_6 = \hat{f}_6 \hat{Q}_0 + \hat{f}_4 \hat{Q}_2 + \hat{f}_2 \hat{Q}_4 + \hat{f}_0 \hat{Q}_6 \tag{2.42}
$$

with

$$
\begin{aligned}
\hat{f}_6 =& \frac{1}{504000} \xi \big(\xi^2 - 1\big)^2 \Big(96 \big(1750\xi^4 + 575\xi^2 + 192 \big) \hat{H}_1^6 \\
&+ 480 \big(125\xi^4 - 86\xi^2 - 42 \big) \hat{H}^2 \hat{H}_3 \hat{H}_1^3 - 72 \big(4375\xi^4 - 550\xi^2 - 1248 \big) \hat{H} \hat{H}_1^4 \hat{H}_2 \\
&- 12 \hat{H}^2 \hat{H}_1^2 \Big[5 \big(125\xi^4 - 173\xi^2 + 36 \big) \hat{H} \hat{H}_4 - 18 \big(625\xi^4 - 520\xi^2 - 248 \big) \hat{H}_2^2 \Big] \\
&+ \hat{H}^3 \Big[- 12 \big(625\xi^4 - 1270\xi^2 + 867 \big) \hat{H}_2^3 + \hat{H} \Big[\big(- 25\xi^4 + 70\xi^2 + 3 \big) \hat{H} \hat{H}_6 \\
&\quad + 8 \big(125\xi^4 - 455\xi^2 + 468 \big) \hat{H}_3^2 \Big] + 12 \big(125\xi^4 - 410\xi^2 + 399 \big) \hat{H} \hat{H}_4 \hat{H}_2 \Big] \\
&+ 24 \hat{H}^3 \hat{H}_1 \Big[\big(25\xi^4 - 55\xi^2 + 36 \big) \hat{H} \hat{H}_5 - 2 \big(625\xi^4 - 1135\xi^2 + 468 \big) \hat{H}_3 \hat{H}_2 \Big] \Big).
\end{aligned} \tag{2.43}
$$

The corresponding solution for $\hat{Q}_6$ was

$$
\hat{Q}_6 = \frac{\hat{I}_2^3 - 2\hat{I}_0 \hat{I}_4 \hat{I}_2 + \hat{I}_0^2 \hat{I}_6}{\hat{I}_0^4} \tag{2.44}
$$

with

$$
\begin{aligned}
\hat{I}_6 = \frac{1}{10500} \int_{-1/2}^{1/2} \Big[& 128 \hat{H}_1^6 - 136 \hat{H}^2 \hat{H}_3 \hat{H}_1^3 - 1176 \hat{H} \hat{H}_1^4 \hat{H}_2 \\
&+ 4 \hat{H}^2 \hat{H}_1^2 \Big(23 \hat{H} \hat{H}_4 - 108 \hat{H}_2^2 \Big) \\
&+ \hat{H}^3 \Big(207 \hat{H}_2^3 + \hat{H} \big(\hat{H} \hat{H}_6 - 58 \hat{H}_3^2 \big) - 76 \hat{H} \hat{H}_4 \hat{H}_2 \Big)
\end{aligned}
$$

$$+ 2\hat{H}^3\hat{H}_1\Big(300\hat{H}_3\hat{H}_2 - 7\hat{H}\hat{H}_5\Big)\Big]\hat{H}^{-3}\mathrm{d}\eta. \tag{2.45}$$

2.3.5 Eighth-order solution

The partial differential equation for $n = 8$ was

$$\begin{aligned}
&\partial_{0,4}\hat{\psi}_8 + \hat{H}^2\Big[2\partial_{2,2}\hat{\psi}_6 + 3\xi\hat{H}_2^2\Big(2\partial_{0,1}\hat{\psi}_4 + \xi\,\partial_{0,2}\hat{\psi}_4\Big)\Big] \\
&\quad + \xi\hat{H}_1^4\Big[\xi\Big(\xi^2\partial_{0,4}\hat{\psi}_4 + 12\xi\partial_{0,3}\hat{\psi}_4 + 36\partial_{0,2}\hat{\psi}_4\Big) + 24\partial_{0,1}\hat{\psi}_4\Big] \\
&\quad + 2\hat{H}_1^2\Big[\xi^2\partial_{0,4}\hat{\psi}_6 + 6\xi\partial_{0,3}\hat{\psi}_6 + 6\partial_{0,2}\hat{\psi}_6 \\
&\qquad - 3\xi\hat{H}\hat{H}_2\Big(\xi^2\partial_{0,3}\hat{\psi}_4 + 6\xi\partial_{0,2}\hat{\psi}_4 + 6\partial_{0,1}\hat{\psi}_4\Big) \\
&\qquad + 3\xi\hat{H}^2\Big(2\partial_{2,1}\hat{\psi}_4 + \xi\,\partial_{2,2}\hat{\psi}_4\Big)\Big] \\
&\quad + 4\hat{H}\hat{H}_1\Big(-2\partial_{1,2}\hat{\psi}_6 - \xi\partial_{1,3}\hat{\psi}_6 + \xi\hat{H}\Big[\hat{H}_3\Big(2\partial_{0,1}\hat{\psi}_4 + \xi\partial_{0,2}\hat{\psi}_4\Big) \\
&\qquad + 3\hat{H}_2\Big(2\partial_{1,1}\hat{\psi}_4 + \xi\partial_{1,2}\hat{\psi}_4\Big)\Big] - \xi\hat{H}^2\partial_{3,1}\hat{\psi}_4\Big) \\
&\quad + \hat{H}^4\partial_{4,0}\hat{\psi}_4 \\
&\quad = \hat{H}\Big[2\hat{H}_2\Big(2\partial_{0,2}\hat{\psi}_6 + \xi\partial_{0,3}\hat{\psi}_6\Big) \\
&\qquad + 4\xi\hat{H}_1^3\Big(\xi^2\partial_{1,3}\hat{\psi}_4 + 6\xi\partial_{1,2}\hat{\psi}_4 + 6\partial_{1,1}\hat{\psi}_4\Big) \\
&\qquad + \xi\hat{H}^2\Big(\hat{H}_4\partial_{0,1}\hat{\psi}_4 + 4\hat{H}_3\partial_{1,1}\hat{\psi}_4 + 6\hat{H}_2\partial_{2,1}\hat{\psi}_4\Big)\Big],
\end{aligned} \tag{2.46}$$

and the solution for $\hat{\psi}_8$ was

$$\hat{\psi}_8 = \hat{f}_8\hat{Q}_0 + \hat{f}_6\hat{Q}_2 + \hat{f}_4\hat{Q}_4 + \hat{f}_2\hat{Q}_6 + \hat{f}_0\hat{Q}_8 \tag{2.47}$$

with

$$\begin{aligned}
\hat{f}_8 = &-\frac{1}{1552320000}\xi\left(\xi^2-1\right)^2 \\
&\times\Big(1152\left(459375\xi^6 + 177625\xi^4 + 84800\xi^2 + 31168\right)\hat{H}_1^8
\end{aligned}$$

$$
\begin{aligned}
&+ 384\left(857500\xi^6 - 335125\xi^4 - 423240\xi^2 - 112572\right)\hat{H}^2\hat{H}_3\hat{H}_1^5 \\
&- 576\left(2572500\xi^6 + 91875\xi^4 - 542400\xi^2 - 560752\right)\hat{H}\hat{H}_1^6\hat{H}_2 \\
&- 48\hat{H}^2\hat{H}_1^4\Big[\left(1071875\xi^6 - 984375\xi^4 - 559520\xi^2 + 418272\right)\hat{H}\hat{H}_4 \\
&\qquad - 42\left(612500\xi^6 - 280625\xi^4 - 358320\xi^2 - 83256\right)\hat{H}_2^2\Big] \\
&+ 192\hat{H}^3\hat{H}_1^3\Big[5\left(6125\xi^6 - 9695\xi^4 - 72\xi^2 + 5316\right)\hat{H}\hat{H}_5 \\
&\qquad - 2\left(1071875\xi^6 - 1176875\xi^4 - 660060\xi^2 + 731706\right)\hat{H}_3\hat{H}_2\Big] \\
&- 8\hat{H}^3\hat{H}_1^2\Big[36\left(1071875\xi^6 - 1273125\xi^4 - 719735\xi^2 + 1054259\right)\hat{H}_2^3 \\
&\qquad + \hat{H}\Big(\left(61250\xi^6 - 148925\xi^4 + 96960\xi^2 - 16437\right)\hat{H}\hat{H}_6 \\
&\qquad\qquad - 168\left(21875\xi^6 - 45625\xi^4 + 6720\xi^2 + 30784\right)\hat{H}_3^2\Big) \\
&\qquad - 36\left(153125\xi^6 - 300125\xi^4 + 34995\xi^2 + 195787\right)\hat{H}\hat{H}_4\hat{H}_2\Big] \\
&+ \hat{H}^4\Big[72\left(153125\xi^6 - 357875\xi^4 + 98685\xi^2 + 196733\right)\hat{H}_2^4 \\
&\qquad - 12\left(306250\xi^6 - 1148875\xi^4 + 1814040\xi^2 - 2077431\right)\hat{H}\hat{H}_4\hat{H}_2^2 \\
&\qquad + 8\hat{H}\Big(\left(12250\xi^6 - 62125\xi^4 + 128820\xi^2 - 91569\right)\hat{H}\hat{H}_6 \\
&\qquad\qquad + \left(-612500\xi^6 + 2413250\xi^4 - 4164000\xi^2 + 4989234\right)\hat{H}_3^2\Big)\hat{H}_2 \\
&\qquad + \hat{H}^2\Big(\left(-875\xi^6 + 4025\xi^4 + 2655\xi^2 - 22893\right)\hat{H}\hat{H}_8 \\
&\qquad\qquad + 2\left(61250\xi^6 - 387625\xi^4 + 911180\xi^2 - 476853\right)\hat{H}_4^2 \\
&\qquad\qquad + 16\left(12250\xi^6 - 73675\xi^4 + 169080\xi^2 - 92823\right)\hat{H}_3\hat{H}_5\Big)\Big] \\
&+ 16\hat{H}^4\hat{H}_1\Big[3\left(-61250\xi^6 + 195125\xi^4 - 201240\xi^2 + 140517\right)\hat{H}\hat{H}_5\hat{H}_2 \\
&\qquad + 180\left(30625\xi^6 - 67725\xi^4 + 15909\xi^2 + 46259\right)\hat{H}_3\hat{H}_2^2 \\
&\qquad + \hat{H}\Big(\left(1750\xi^6 - 6125\xi^4 + 8440\xi^2 - 16881\right)\hat{H}\hat{H}_7 \\
&\qquad\qquad - 35\left(8750\xi^6 - 31175\xi^4 + 36084\xi^2 - 27579\right)\hat{H}_3\hat{H}_4\Big)\Big]\Big). \qquad (2.48)
\end{aligned}
$$

The corresponding solution for $\hat{Q}_8$ was

$$
\hat{Q}_8 = \frac{\hat{I}_2^4 - 3\hat{I}_0\hat{I}_4\hat{I}_2^2 + 2\hat{I}_0^2\hat{I}_6\hat{I}_2 + \hat{I}_0^2\hat{I}_4^2 - \hat{I}_0^3\hat{I}_8}{\hat{I}_0^5} \qquad (2.49)
$$

with

$$\begin{aligned}\hat{I}_8 = \frac{1}{72765000}\int_{-1/2}^{1/2}\Big[&398016\hat{H}_1^8 - 2408400\hat{H}^2\hat{H}_3\hat{H}_1^5 - 6462576\hat{H}\hat{H}_1^6\hat{H}_2\\ &+ 144\hat{H}^2\hat{H}_1^4\Big(5386\hat{H}\hat{H}_4 - 84657\hat{H}_2^2\Big)\\ &+ 36\hat{H}^3\hat{H}_1^3\Big(248032\hat{H}_3\hat{H}_2 - 1059\hat{H}\hat{H}_5\Big)\\ &- 6\hat{H}^3\hat{H}_1^2\Big[-1408779\hat{H}_2^3 + \hat{H}\Big(1891\hat{H}\hat{H}_6 + 46202\hat{H}_3^2\Big)\\ &\quad + 69708\hat{H}\hat{H}_4\hat{H}_2\Big]\\ &+ \hat{H}^4\Big[-101169\hat{H}_2^4 - 598284\hat{H}\hat{H}_4\hat{H}_2^2\\ &\quad + 4\hat{H}\Big(7147\hat{H}\hat{H}_6 - 238641\hat{H}_3^2\Big)\hat{H}_2\\ &\quad + 2\hat{H}^2\Big(62\hat{H}\hat{H}_8 + 26827\hat{H}_4^2 + 39028\hat{H}_3\hat{H}_5\Big)\Big]\\ &+ 4\hat{H}^4\hat{H}_1\Big(770\hat{H}_7\hat{H}^2 - 36621\hat{H}_5\hat{H}\hat{H}_2\\ &\quad - 79746\hat{H}_3\hat{H}_4\hat{H} - 220014\hat{H}_3\hat{H}_2^2\Big)\Big]\hat{H}^{-3}\mathrm{d}\eta. \end{aligned} \tag{2.50}$$

2.3.6 Tenth-order solution

The partial differential equation for $n = 10$ was

$$\begin{aligned}&\partial_{0,4}\hat{\psi}_{10} + \hat{H}^2\Big[2\partial_{2,2}\hat{\psi}_8 + 3\xi\hat{H}_2^2\big(2\partial_{0,1}\hat{\psi}_6 + \xi\partial_{0,2}\hat{\psi}_6\big)\Big]\\ &\quad + \xi\hat{H}_1^4\Big[\xi\big(\xi^2\partial_{0,4}\hat{\psi}_6 + 12\xi\partial_{0,3}\hat{\psi}_6 + 36\partial_{0,2}\hat{\psi}_6\big) + 24\partial_{0,1}\hat{\psi}_6\Big]\\ &\quad + 2\hat{H}_1^2\Big[\xi^2\partial_{0,4}\hat{\psi}_8 + 6\xi\partial_{0,3}\hat{\psi}_8 + 6\partial_{0,2}\hat{\psi}_8\\ &\qquad - 3\xi\hat{H}\hat{H}_2\big(\xi^2\partial_{0,3}\hat{\psi}_6 + 6\xi\partial_{0,2}\hat{\psi}_6 + 6\partial_{0,1}\hat{\psi}_6\big)\\ &\qquad + 3\xi\hat{H}^2\big(2\partial_{2,1}\hat{\psi}_6 + \xi\partial_{2,2}\hat{\psi}_6\big)\Big]\\ &\quad + 4\hat{H}\hat{H}_1\Big[-2\partial_{1,2}\hat{\psi}_8 - \xi\partial_{1,3}\hat{\psi}_8\\ &\qquad + \xi\hat{H}\big[\hat{H}_3\big(2\partial_{0,1}\hat{\psi}_6 + \xi\partial_{0,2}\hat{\psi}_6\big) + 3\hat{H}_2\big(2\partial_{1,1}\hat{\psi}_6 + \xi\partial_{1,2}\hat{\psi}_6\big)\big]\\ &\qquad - \xi\hat{H}^2\partial_{3,1}\hat{\psi}_6\Big]\\ &\quad + \hat{H}^4\partial_{4,0}\hat{\psi}_6\end{aligned}$$

$$
\begin{aligned}
&= \hat{H}\Big[2\hat{H}_2\big(2\partial_{0,2}\hat{\psi}_8 + \xi\partial_{0,3}\hat{\psi}_8\big) \\
&\quad + 4\xi\hat{H}_1^3\big(\xi^2\partial_{1,3}\hat{\psi}_6 + 6\xi\partial_{1,2}\hat{\psi}_6 + 6\partial_{1,1}\hat{\psi}_6\big) \\
&\quad + \xi\hat{H}^2\big(\hat{H}_4\partial_{0,1}\hat{\psi}_6 + 4\hat{H}_3\partial_{1,1}\hat{\psi}_6 + 6\hat{H}_2\partial_{2,1}\hat{\psi}_6\big)\Big].
\end{aligned} \tag{2.51}
$$

and the solution for $\hat{\psi}_{10}$ was

$$
\hat{\psi}_{10} = \hat{f}_{10}\hat{Q}_0 + \hat{f}_8\hat{Q}_2 + \hat{f}_6\hat{Q}_4 + \hat{f}_4\hat{Q}_6 + \hat{f}_2\hat{Q}_8 + \hat{f}_0\hat{Q}_{10} \tag{2.52}
$$

with

$$
\begin{aligned}
\hat{f}_{10} =& \frac{1}{605404800000}\xi\left(\xi^2-1\right)^2 \\
&\times \Big(13824\left(15159375\xi^8 + 6431250\xi^6 + 3584000\xi^4 + 1873600\xi^2 + 718976\right)\hat{H}_1^{10} \\
&- 3456\left(227390625\xi^8 + 31972500\xi^6 - 26684000\xi^4 - 47202400\xi^2 - 39851712\right) \\
&\quad \times \hat{H}\hat{H}_2\hat{H}_1^8 \\
&+ 9216\left(20671875\xi^8 - 4042500\xi^6 - 8879875\xi^4 - 7016270\xi^2 - 875717\right) \\
&\quad \times \hat{H}^2\hat{H}_3\hat{H}_1^7 \\
&- 1152\hat{H}^2\Big[\\
&\quad 6\left(-144703125\xi^8 + 33871250\xi^6 + 71966000\xi^4 + 57658400\xi^2 + 4216848\right)\hat{H}_2^2 \\
&\quad + \left(28940625\xi^8 - 17364375\xi^6 - 18642250\xi^4 - 4761410\xi^2 + 11257462\right)\hat{H}\hat{H}_4 \\
&\quad \Big]\hat{H}_1^6 \\
&+ 2304\hat{H}^3\Big[\left(1929375\xi^8 - 2113125\xi^6 - 1261450\xi^4 + 857920\xi^2 + 1209186\right)\hat{H}\hat{H}_5 \\
&\quad - 6\left(28940625\xi^8 - 20151250\xi^6 - 22106750\xi^4 - 4527735\xi^2 + 17660196\right)\hat{H}_2\hat{H}_3 \\
&\quad \Big]\hat{H}_1^5 \\
&- 48\hat{H}^3\Big[\\
&\quad 36\left(289406250\xi^8 - 215446875\xi^6 - 242054375\xi^4 - 40498225\xi^2 + 237892709\right)\hat{H}_2^3 \\
&\quad - 12\left(96468750\xi^8 - 123571875\xi^6 - 73253125\xi^4 + 73474795\xi^2 + 77895771\right)
\end{aligned}
$$

$$
\begin{aligned}
&\times \hat{H}\hat{H}_4\hat{H}_2 \\
&+ \hat{H}\Big(\left(9646875\xi^8 - 16537500\xi^6 - 2378000\xi^4 + 14844560\xi^2 - 3137439\right) \hat{H}\hat{H}_6 \\
&\quad - 16\left(48234375\xi^8 - 64771875\xi^6 - 38335250\xi^4\right. \\
&\qquad \left. +41775710\xi^2 + 41678022\right) \hat{H}_3^2 \Big) \\
&\Big] \hat{H}_1^4 \\
+ 192\hat{H}^4 &\Big[\\
&60\left(19293750\xi^8 - 27103125\xi^6 - 16317875\xi^4 + 21635945\xi^2 + 16725957\right) \\
&\quad \times \hat{H}_3\hat{H}_2^2 \\
&+ 3\left(-9646875\xi^8 + 19722500\xi^6 + 1269100\xi^4 - 23953920\xi^2 + 15839739\right) \\
&\quad \times \hat{H}\hat{H}_5\hat{H}_2 \\
&+ \hat{H}\Big(3\left(65625\xi^8 - 164500\xi^6 + 66550\xi^4 + 168900\xi^2 - 326399\right) \hat{H}\hat{H}_7 \\
&\quad - 5\left(9646875\xi^8 - 21315000\xi^6 - 728950\xi^4\right. \\
&\qquad \left. +28438816\xi^2 - 21337101\right) \hat{H}_3\hat{H}_4 \Big) \\
&\Big] \hat{H}_1^3 \\
- 12\hat{H}^4 &\Big[\\
&- 72\left(96468750\xi^8 - 141487500\xi^6 - 87956125\xi^4\right. \\
&\quad \left. +135287650\xi^2 + 72200289\right) \hat{H}_2^4 \\
&+ 36\left(48234375\xi^8 - 110556250\xi^6 - 238750\xi^4\right. \\
&\quad \left. +177654830\xi^2 - 200028157\right) \hat{H}\hat{H}_4\hat{H}_2^2 \\
&- 8\hat{H}\Big(\\
&\quad \left(4134375\xi^8 - 12752250\xi^6 + 8138150\xi^4\right. \\
&\qquad \left. +14923030\xi^2 - 43155369\right) \hat{H}\hat{H}_6 \\
&\quad - 6\left(48234375\xi^8 - 114537500\xi^6 + 1773000\xi^4\right. \\
&\qquad \left. +196787840\xi^2 - 235828467\right) \hat{H}_3^2 \Big) \hat{H}_2 \\
&+ \hat{H}^2\Big(\\
\end{aligned}
$$

$$
\begin{aligned}
&\quad - 6\left(6890625\xi^8 - 24438750\xi^6 + 18752750\xi^4\right.\\
&\qquad \left.+30232570\xi^2 - 95120683\right)\hat{H}_4^2\\
&\quad - 80\left(826875\xi^8 - 2837100\xi^6 + 2095370\xi^4\right.\\
&\qquad \left.+3470572\xi^2 - 10727589\right)\hat{H}_3\hat{H}_5\\
&\quad + 3\left(65625\xi^8 - 232750\xi^6 + 266100\xi^4\right.\\
&\qquad \left.+95710\xi^2 - 1625853\right)\hat{H}\hat{H}_8\Big)\\
&\Big]\hat{H}_1^2\\
&+ 8\hat{H}^5\Big[\\
&\quad - 72\left(48234375\xi^8 - 118518750\xi^6 + 2283250\xi^4\right.\\
&\qquad \left.+243720050\xi^2 - 364658077\right)\hat{H}_3\hat{H}_2^3\\
&\quad + 36\left(4134375\xi^8 - 14663250\xi^6 + 12953350\xi^4\right.\\
&\qquad \left.+16786190\xi^2 - 42792513\right)\hat{H}\hat{H}_5\hat{H}_2^2\\
&\quad - 12\hat{H}\Big[\left(196875\xi^8 - 903000\xi^6 + 1532800\xi^4 - 1891540\xi^2 + 3981057\right)\hat{H}\hat{H}_7\\
&\qquad - 6\left(6890625\xi^8 - 26031250\xi^6 + 25577750\xi^4\right.\\
&\qquad\quad \left.+29344670\xi^2 - 72913563\right)\hat{H}_3\hat{H}_4\Big]\hat{H}_2\\
&\quad + \hat{H}\Big(\\
&\qquad 80\left(1378125\xi^8 - 5365500\xi^6 + 5655050\xi^4\right.\\
&\qquad\quad \left.+5880244\xi^2 - 13913847\right)\hat{H}_3^3\\
&\qquad - 12\left(459375\xi^8 - 2425500\xi^6 + 4703200\xi^4\right.\\
&\qquad\quad \left.-7378720\xi^2 + 18299277\right)\hat{H}\hat{H}_6\hat{H}_3\\
&\qquad + \hat{H}\Big[5\left(2625\xi^8 - 12950\xi^6 + 27960\xi^4 - 181666\xi^2 + 416671\right)\hat{H}\hat{H}_9\\
&\qquad\quad - 6\left(1378125\xi^8 - 7754250\xi^6 + 15785300\xi^4\right.\\
&\qquad\qquad \left.-26243510\xi^2 + 66543231\right)\hat{H}_4\hat{H}_5\Big]\Big)\\
&\quad \Big]\hat{H}_1\\
&- \hat{H}^5\Big[
\end{aligned}
$$

$$
\begin{aligned}
&216\left(9646875\xi^8-24500000\xi^6+269125\xi^4+61417450\xi^2-100483194\right)\hat{H}_2^5\\
&-720\left(1378125\xi^8-5365500\xi^6+5651475\xi^4+3873954\xi^2-2215966\right)\hat{H}\hat{H}_4\hat{H}_2^3\\
&+72\hat{H}\Big(5\left(91875\xi^8-501025\xi^6+1234115\xi^4-2835687\xi^2+4460866\right)\hat{H}\hat{H}_6\\
&\quad-4\left(6890625\xi^8-27623750\xi^6+30472250\xi^4\right.\\
&\qquad\left.+16393290\xi^2+5007657\right)\hat{H}_3^2\Big)\hat{H}_2^2\\
&-12\hat{H}^2\Big(\\
&\quad-5\left(1378125\xi^8-8470875\xi^6+24694525\xi^4-64110781\xi^2+91602798\right)\hat{H}_4^2\\
&\quad-8\left(1378125\xi^8-8232000\xi^6+23152400\xi^4\right.\\
&\qquad\left.-58865060\xi^2+85653543\right)\hat{H}_3\hat{H}_5\\
&\quad+\left(39375\xi^8-273875\xi^6+900075\xi^4-1980025\xi^2+1332594\right)\hat{H}\hat{H}_8\Big)\hat{H}_2\\
&+\hat{H}^2\Big(\\
&\quad16\left(6890625\xi^8-43548750\xi^6+138297500\xi^4\right.\\
&\qquad\left.-381048170\xi^2+499790907\right)\hat{H}_4\hat{H}_3^2\\
&\quad-32\left(39375\xi^8-330750\xi^6+1233200\xi^4\right.\\
&\qquad\left.-1698770\xi^2-777423\right)\hat{H}\hat{H}_7\hat{H}_3\\
&\quad+\hat{H}\Big(-120\left(11025\xi^8-105350\xi^6+418200\xi^4-448210\xi^2-589233\right)\hat{H}_5^2\\
&\qquad-200\left(11025\xi^8-102165\xi^6+400117\xi^4\right.\\
&\qquad\qquad\left.-452383\xi^2-500274\right)\hat{H}_4\hat{H}_6\\
&\qquad+\left(2625\xi^8-17500\xi^6-34050\xi^4+489940\xi^2-845239\right)\hat{H}\hat{H}_{10}\Big)\\
&\quad\Big]\\
&\Big).
\end{aligned}
\tag{2.53}
$$

The corresponding solution for $\hat{Q}_10$ was

$$
\hat{Q}_{10}=\frac{\hat{I}_2^5-4\hat{I}_0\hat{I}_4\hat{I}_2^3+3\hat{I}_0^2\hat{I}_6\hat{I}_2^2+3\hat{I}_0^2\hat{I}_4^2\hat{I}_2-2\hat{I}_0^3\hat{I}_8\hat{I}_2-2\hat{I}_0^3\hat{I}_4\hat{I}_6+\hat{I}_0^4\hat{I}_{10}}{\hat{I}_0^6}
\tag{2.54}
$$

with

$$\begin{aligned}\hat{I}_{10} = \frac{1}{2364862500}\int_{-1/2}^{1/2}\Big[\,&7649856\hat{H}_1^{10} - 111217608\hat{H}^2\hat{H}_3\hat{H}_1^7 - 184424472\hat{H}\hat{H}_1^8\hat{H}_2\\
&+ 36\hat{H}^2\hat{H}_1^6\big(680569\hat{H}\hat{H}_4 - 21657984\hat{H}_2^2\big)\\
&+ 18\hat{H}^3\hat{H}_1^5\big(103265\hat{H}\hat{H}_5 + 21611188\hat{H}_3\hat{H}_2\big)\\
&+ 3\hat{H}^3\hat{H}_1^4\big[191866041\hat{H}_2^3 + \hat{H}\big(11130458\hat{H}_3^2 - 412337\hat{H}\hat{H}_6\big)\\
&\qquad + 13976700\hat{H}\hat{H}_4\hat{H}_2\big]\\
&+ 12\hat{H}^4\hat{H}_1^3\big(8636\hat{H}_7\hat{H}^2 - 1749939\hat{H}_5\hat{H}\hat{H}_2 - 3497158\hat{H}_3\hat{H}_4\hat{H}\\
&\qquad + 22649052\hat{H}_3\hat{H}_2^2\big)\\
&+ \hat{H}^4\hat{H}_1^2\Big[133697655\hat{H}_2^4 - 131823180\hat{H}\hat{H}_4\hat{H}_2^2\\
&\qquad + 12\hat{H}\big(262657\hat{H}\hat{H}_6 - 16541011\hat{H}_3^2\big)\hat{H}_2\\
&\qquad + 2\hat{H}^2\big(-28914\hat{H}\hat{H}_8 + 2806627\hat{H}_4^2 + 4151352\hat{H}_3\hat{H}_5\big)\Big]\\
&+ \hat{H}^5\Big[-34502625\hat{H}_2^5 + 9362016\hat{H}\hat{H}_4\hat{H}_2^3\\
&\qquad + \hat{H}\big(2316753\hat{H}\hat{H}_6 + 76988\hat{H}_3^2\big)\hat{H}_2^2\\
&\qquad + \hat{H}^2\big(-52200\hat{H}\hat{H}_8 + 9040251\hat{H}_4^2 + 13154788\hat{H}_3\hat{H}_5\big)\hat{H}_2\\
&\qquad - 2\hat{H}^2\Big(53612\hat{H}\hat{H}_7\hat{H}_3 - 7289089\hat{H}_4\hat{H}_3^2\\
&\qquad\qquad + \hat{H}\big(623\hat{H}\hat{H}_{10} + 50882\hat{H}_5^2 + 86869\hat{H}_4\hat{H}_6\big)\Big)\Big]\\
&+ 2\hat{H}^5\hat{H}_1\Big(8603802\hat{H}\hat{H}_5\hat{H}_2^2 - 150844032\hat{H}_3\hat{H}_2^3\\
&\qquad + 2\hat{H}\big(48651\hat{H}\hat{H}_7 + 17077496\hat{H}_3\hat{H}_4\big)\hat{H}_2\\
&\qquad + \hat{H}\big(-10634\hat{H}^2\hat{H}_9 + 8348120\hat{H}_3^3 + 550452\hat{H}\hat{H}_6\hat{H}_3\\
&\qquad\qquad + 1013437\hat{H}\hat{H}_4\hat{H}_5\big)\Big)\Big]\hat{H}^{-3}\mathrm{d}\eta. \qquad (2.55)\end{aligned}$$

Chapter 3

Simulations

We simulated flow in the same expansion–contraction microchannel geometry described in Chapter 3 using dissipative particle dynamics (DPD). DPD is a mesoscopic particle-based simulation method that can simulate complex fluids and hydrodynamic behavior[43] with less computational cost than more detailed models, such as atomistic molecular dynamics.[44] DPD simulates soft particles that can be thought of as collections of smaller particles or molecules. Their motion is governed by pairwise interactions that include conservative $\mathbf{F}_{\mathrm{C}}$, dissipative $\mathbf{F}_{\mathrm{D}}$, and random $\mathbf{F}_{\mathrm{R}}$ forces.[39] The conservative force acting on the particle i due to particle j is a soft repulsion:[39]

$$\mathbf{F}_{\mathrm{C}} = \begin{cases} a_{ij}\left(1 - \dfrac{r}{r_{\mathrm{c}}}\right)\hat{\mathbf{r}}, & r \leq r_{\mathrm{c}} \\ 0, & r > r_{\mathrm{c}} \end{cases}, \tag{3.1}$$

where a_{ij} sets the strength of the repulsion between particle i and j, r is the distance between the centers of particle i and j, $\hat{\mathbf{r}}$ is the unit vector to the center of the particle i from the center of particle j, and r_{c} is the cutoff radius of the interaction setting the effective size of the particles.[45] The random and dissipative forces impart thermal fluctuations and drag while conserving momentum. These forces are given by[39]

$$\mathbf{F}_{\mathrm{D}} = -\gamma_{ij} w(r)(\hat{\mathbf{r}} \cdot \Delta\mathbf{v})\hat{\mathbf{r}} \tag{3.2}$$

$$\mathbf{F}_{\mathrm{R}} = \sqrt{\gamma_{ij} w(r)}\,\xi(\hat{\mathbf{r}}), \tag{3.3}$$

where γ_{ij} is the drag coefficient between the particles i and j, w is a weight function, and $\Delta\mathbf{v}$ is the difference in the velocities of particles i and j. To satisfy the fluctuation–dissipation

theorem,[46] ξ is an independent Gaussian-distributed random variable for a pair of particles having mean $\langle \xi(t) \rangle = 0$ and variance $\langle \xi(t)\xi(t') \rangle = 2k_{\mathrm{B}}T\delta(t-t')$, where T is the temperature and k_{B} is the Boltzmann constant.[45]

In our simulations, the DPD particles had nominal diameter d and mass m. We used a generalized weight function proposed by Fan *et al.*,[45,47]

$$w(r) = \begin{cases} \left(1 - \dfrac{r}{r_{\mathrm{c}}}\right)^{1/2}, & r \leq r_{\mathrm{c}} \\ 0, & r > r_{\mathrm{c}} \end{cases}. \tag{3.4}$$

We used typical DPD parameters: cutoff $r_c = 1.0d$, density $\rho = 3d^{-3}$, interaction parameter $25k_{\mathrm{B}}T/d$, and friction coefficient of $4.5m/\tau$, where $\tau = \sqrt{md^2/(k_{\mathrm{B}}T)}$ is the unit of time.[45] With these parameters, the Schmidt number of the DPD fluid is estimated to be 4.1 using the approximation proposed by Fan *et al.*,[47] meaning the fluid is liquid-like. All simulations were performed using HOOMD-blue (version 5.3.0) extended with azplugins (version 1.1.0).[48–51] Newton's equations were integrated with a velocity Verlet scheme with timestep $0.01\,\tau$.

A simulation in a given microchannel geometry was initialized as follows. First, DPD particles were randomly dispersed into a three-dimensional box with periodic boundary conditions at the chosen density. The box length was L in the x direction, the expansion width plus a padding of $4\,d$ on both sides in the y direction, and $D = 30\,d$ in the z direction. This bulk fluid was equilibrated for $10^3\tau$.

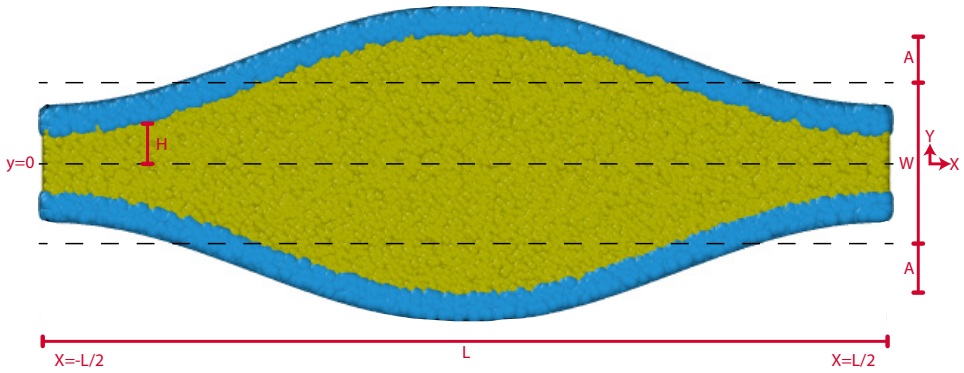

Figure 3.1: DPD model of same sinusoidal microchannel as Figure 2.1.

Next, the bulk fluid was converted to represent a solvent and the microchannel walls. Particles inside the microchannel were converted to be solvent particles, and their center-of-mass velocity was zeroed. Particles outside the microchannel but within $3\,d$ in the y direction were converted to be wall particles, and their velocities were all set to zero. The other particles were not needed and so removed (Figure 3.1). A bounce-back rule was applied to the solvent particles[43,52] to help enforce the no-slip and no-penetration boundary conditions at the walls; the point of intersection for a solvent particle with the wall was found numerically using a combination of Newton's method and bisection search. The presence of explicit wall particles helps reduce slip and undesirable density oscillations.[43,45,53] The new configuration was equilibrated for $10^3\tau$, then flow was generated by applying a constant body force $F = 0.001 k_\mathrm{B}T/d$ in the x direction for all solvent particles. The flow was allowed to develop for $10^4\tau$, then measurements of the flow velocity and volumetric flow rate were taken during a production period of $10^5\tau$.

The one-dimensional flow field $u_x(y)$ at the expansion and contraction of the microchannel was measured using histogramming every $10\,\tau$. Particles with an x coordinate within a thickness $0.5\,d$ centered at the expansion were binned with respect to their y coordinate between the walls using a bin size of $0.5\,d$, and the velocities of particles in each bin were averaged. The same procedure was used at the contraction, but due to the simulation geometry, particles were binned and averaged in two separate half-thicknesses at each end of the simulation box, then the resulting profiles were averaged together with equal weight.

For a given cross-section of the microchannel (normal in the x direction), the volumetric flow rate is $Q = AU_x$, where A is the cross-sectional area and U_x is the average x-velocity. The DPD fluid is not perfectly incompressible, so Q can vary with respect to x. However, we expect the corresponding mass flow rate to be independent of x at steady state. Accordingly, we sought to compute an average Q for the microchannel conveniently using particle-level information. We define the volumetric flow rate as

$$Q = \frac{\int \mathrm{d}x \rho^{(1)}(x) A(x) U_x(x)}{\int \mathrm{d}x \rho^{(1)}(x)}, \tag{3.5}$$

where $\rho^{(1)}$ is the probability density function to find a particle at x, and the x dependence of A and U_x is emphasized. (Note that if the flow is incompressible and $\rho^{(1)}$ is uniform, this definition reduces to a simple average.) The average velocity across the cross-section at x can also be computed as

$$U_x(x) = \frac{\int \mathrm{d}y\mathrm{d}z\mathrm{d}v_x \rho^{(1)}(x,y,z,v_x) v_x}{\int \mathrm{d}y\mathrm{d}z\mathrm{d}v_x \rho^{(1)}(x,y,z,v_x)}, \tag{3.6}$$

where $\rho^{(1)}(x,y,z,v_x)$ is the probability density function for finding a particle at a particular position with velocity v_x. Using the fact that

$$\rho^{(1)}(x) = \int \mathrm{d}y\mathrm{d}z\mathrm{d}v_x \rho^{(1)}(x,y,z,v_x), \tag{3.7}$$

and combining, we get

$$Q = \frac{\int \mathrm{d}x\mathrm{d}y\mathrm{d}z\mathrm{d}v_x \rho^{(1)}(x,y,z,v_x) A(x) v_x}{\int \mathrm{d}x\mathrm{d}y\mathrm{d}z\mathrm{d}v_x \rho^{(1)}(x,y,z,v_x)}. \tag{3.8}$$

Hence, Q can be computed from an ensemble average of the particle positions and velocities, $Q = \langle A(x) v_x \rangle$. We performed this average in our simulation by sampling all solvent particles every $10^2\,\tau$.

The viscosity μ of the DPD fluid is needed to compare our simulated u_x and Q with the theoretical predictions of Chapter 2. We determined this viscosity from the simulated velocity field $u_x(x,y)$ between parallel plates ($A = 0$). We collected this profile using two-dimensional histograms over the whole channel volume with bin size $0.5\,d$ in both dimensions and the same sampling frequency as for the one-dimensional histograms to obtain $u_x(y)$. To improve statistics, this calculation was done for both $L = 150\,d$ and $L = 75\,d$ with $W = D = 30\,d$. The measured flow fields were then averaged over x with equal weight to obtain an average $u_x(y)$. In the parallel-plate geometry, a parabolic flow field is expected, and its gradient is:

$$\frac{\mathrm{d}u_x}{\mathrm{d}y} = -\frac{\rho F}{\mu} y. \tag{3.9}$$

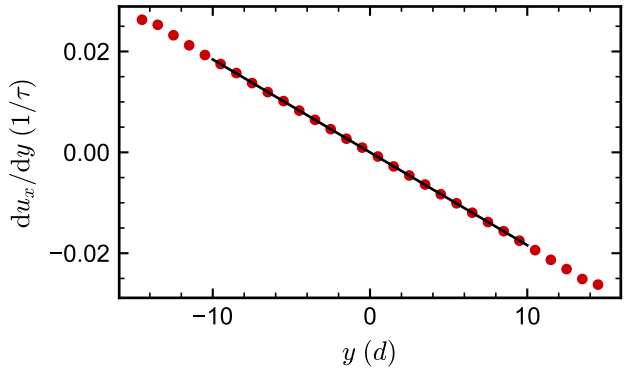

Figure 3.2: Velocity gradient $\mathrm{d}u_x/\mathrm{d}y$ as a function of y in the parallel plate geometry.

Hence, μ can be extracted from a linear fit of $\mathrm{d}u_x/\mathrm{d}y$ as a function of y. Fitting $\mathrm{d}u_x/\mathrm{d}y$, rather than u_x or Q directly, helps avoid ambiguities if a small amount of wall slip is present. We numerically differentiated our measured $u_x(y)$ and noted that a slight amount of slip appears to be present near the walls (Figure 3.2), so we fit a line for $-10\,d \leq y \leq 10\,d$. The slope was $-1.84 \times 10^{-3}(d\tau)^{-1}$, giving an estimated viscosity of $1.63 k_{\mathrm{B}} T\tau/d^3$.

Chapter 4

Results and Discussion

To evaluate the accuracy of our mesoscale particle-based model, we performed simulations in a variety of microchannels. We used a constant average width $W = 30\,d$ for all microchannels. In one set of microchannels had a fixed length of L/W = 2.5 or 5, and the amplitude was varied from A/W = 0 to 0.4 in increments of 0.1. The other set of microchannels held the amplitude constant at A/W = 0.2 or 0.4, and the length was varied as L/W = 1, 1.25, 1.75, 2, 3, 4, and 5.

We first compared the velocity field $u_x(y)$ at the expansion and contraction of the longest microchannel we simulated ($L/W = 5$), for which we expect the theoretical predictions to be the most accurate because the small parameter ($\epsilon = W/L$) used in the perturbation theory is smallest. To facilitate the comparison, we normalized the simulation velocities by the theoretically expected average velocity between parallel plates, $U_{\parallel}$, using the viscosity μ that we measured (Figure 4.1). The maximum velocity at the expansion systematically decreased as A increased; at the contraction, it initially increased before decreasing. The simulated velocities consistently exceeded the theoretical predictions by a small amount, which we believe is likely due to a small amount of wall slip (Figure 3.2). Overall, we still had very good agreement between the simulations and fourth-order theoretical predictions[40] at both points for all microchannel amplitudes.

The velocity at the expansion becomes small for the microchannels with larger amplitudes, so we replotted the same data with u_x normalized by the theoretically predicted average velocity at the expansion U_{e} and contraction U_{c} (Figure 4.2). These average velocities were calculated from the theoretically predicted Q using the cross-sectional area at the expansion and

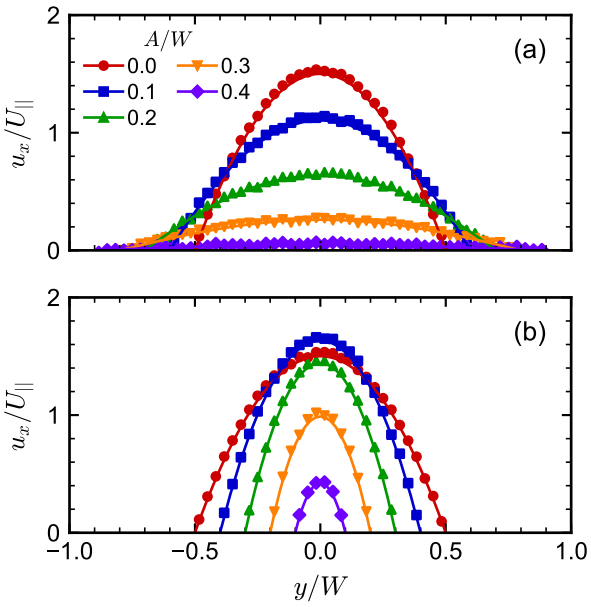

Figure 4.1: Velocity $u_x(y)$ at the (a) expansion and (b) contraction for various amplitudes A at fixed length $L/W = 5$. The velocity is normalized by the expected average velocity between the parallel plates, $U_{\|}$. Symbols are simulation data, and solid lines are theoretical predictions using the fourth-order theoretical solution.

contraction. In this representation, there was more apparent scatter in the data for the larger amplitude channels, suggesting statistical error due to the lower signal-to-noise ratio of these measurements, but there was no apparent systematic error. Figures 4.1 and 4.2 indicate that the DPD simulations are producing the correct flow field for the geometries tested.

We next compared the volumetric flow rate Q measured in the DPD simulations with fourth-order theoretical predictions for microchannels having two different amplitudes ($A/W =$ 0.2 and 0.4) as a function of channel length (Figure 4.3a). For these geometries, Q tended to decrease somewhat as L decreased, qualitatively because the fluid encounters contractions more frequently when the periodic repeat length L is shorter. We confirmed that the simulated volumetric flow rate was in good agreement with the theoretical prediction[40] for the longest lengths, which we expected based on the good agreement in the velocity fields (Figure 4.1). However, we also found that there was good agreement between the simulations and theoretical predictions for $2 \lesssim L/W \leq 5$. To confirm the DPD simulation methods remain accurate for other amplitudes, we also compared Q in two channels with fixed lengths ($L/W = 2.5$ and 5.0) and varied amplitudes (Figure 4.3b). For these geometries, Q decreased as the amplitude increased

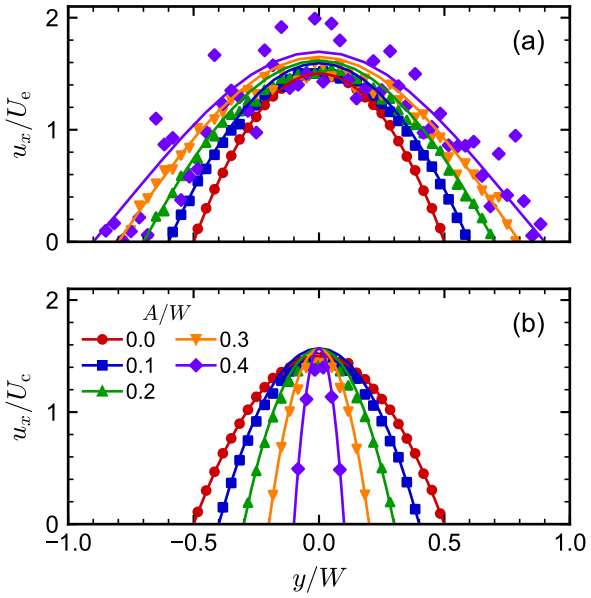

Figure 4.2: Same as Figure 4.1 but normalized using the fourth-order theoretical solution for the average velocity at the (a) expansion U_e and (b) contraction U_c.

due to the enhanced constriction, and the DPD simulations were again in good agreement with the fourth-order theoretical predictions for all amplitudes, with a small overprediction that ranged from 2.5% for $A/W = 0$ to 8.5% for $A/W = 0.4$ for $L/W = 5$.

The theoretical predictions begin to deviate noticeably from the simulations in Figure 4.3 for $L/W \lesssim 2$. We believed this deviation was due to inaccuracy in the theoretical predictions, rather than the simulations, because the small parameter used in the regular perturbation method increases as L/W decreases, potentially making the series expansion less accurate. In support of this notion, we extended the theoretical solution up to the tenth order. Figure 4.4 compares the predictions for Q for varying degrees of approximation to the DPD simulation data. The tenth-order theoretical prediction appears to align better with the DPD simulations to slightly smaller L/W. However, the predicted Q diverged more strongly for the higher-order approximations as $L/W \to 1$, suggesting that the series solution may in fact be divergent in this regime. We noted in exploratory calculations that this problem seemed to be more exacerbated in microchannels with larger amplitude.

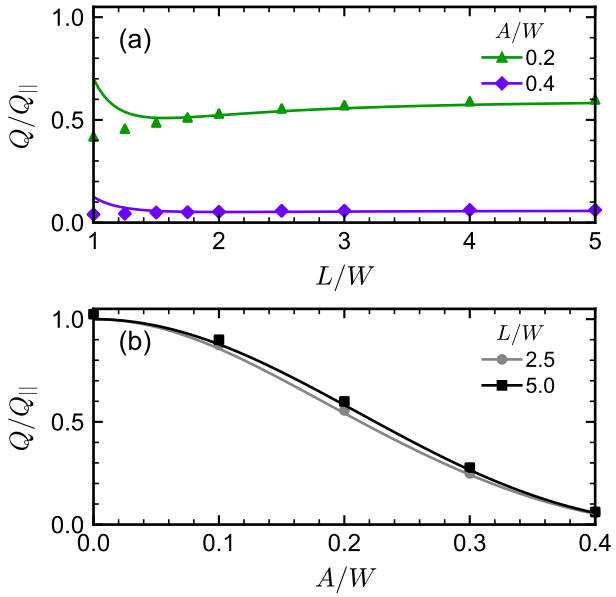

Figure 4.3: Volumetric flow rate Q as a function of (a) length L and (b) amplitude A. Symbols are simulation data, and solid lines are fourth-order theoretical predictions.

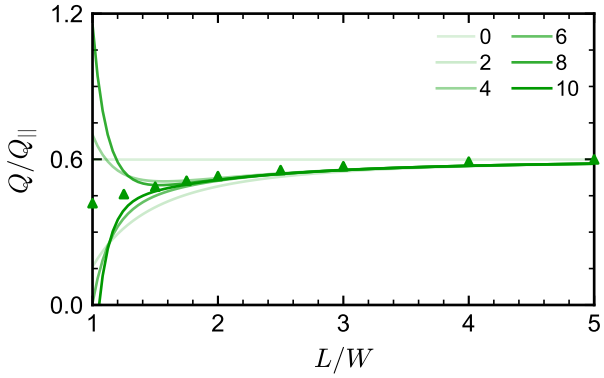

Figure 4.4: Theoretical approximations of varying order for the volumetric flow rate Q as a function of length L for amplitude $A/W = 0.2$. Symbols are simulation data.

Chapter 5

Conclusion

Despite the proven efficacy of polymer flooding in enhancing oil recovery, the mechanisms driving this improved performance, particularly in the role of elastic turbulence, remain poorly understood. In particular, it is unclear how polymer architecture and hydrophobic associations influence the onset and characteristics of elastic turbulence in low Reynolds number flows through expansion–contraction microchannels. This represents a critical knowledge gap, since understanding the molecular-level flow behavior is essential for the rational design of more effective polymers for EOR.

Toward addressing this problem, we performed mesoscale particle-based simulations of a Newtonian fluid flowing in expansion–contraction microchannels at low Reynolds numbers, an approach not previously applied to this geometry. By comparing our results to a theoretical solution, we established the reliability of DPD for simulating flow in this geometry, which may then serve as a baseline for future studies of elastic turbulence. The most notable limitation that we found in our analysis was the inaccuracy of the theoretical model for channels with frequent contractions. A numerical solution, based on a boundary-integral method,[54] could be used to confirm the validity of the DPD simulations in this regime; however, it may be cumbersome to implement. Another mesoscale particle-based simulation method, such as multiparticle collision dynamics,[55] could also be used for validation. However, the success of DPD in modeling flow in longer microchannels suggests that we might expect them to also be reasonably accurate for shorter microchannels. DPD might then be regarded as a convenient computational method for simulating flows in geometries that challenge analytical theory.

Elastic turbulence plays a critical role in polymer flooding, and a deeper understanding of its mechanisms and effects will enable the rational design of polymers tailored for optimal performance. Therefore, the next step in this research is to incorporate polymers into the simulation framework to investigate how molecular structure influences flow behavior. This advancement has the potential to significantly improve oil recovery efficiency and contribute to meeting the growing global energy demand. Ultimately, bridging this molecular-to-macroscale understanding of elastic turbulence will not only advance the science of complex fluid dynamics but also drive innovation in sustainable energy technologies.

References

[1] U.S. Energy Information Administration Oil and petroleum products explained. 2024; https://www.eia.gov/energyexplained/oil-and-petroleum-products/use-of-oil.php, accessed May 27th, 2025.

[2] McKinsey & Company From Crude Oil to Chemicals: How Refineries Can Adapt to Shifting Demand. 2020; https://www.mckinsey.com/industries/chemicals/our-insights/from-crude-oil-to-chemicals-how-refineries-can-adapt-to-shifting-demand, accessed May 23th, 2025.

[3] Administration, U. E. I. EIA Projects U.S. Energy-Related CO2 Emissions to Fall Through 2050. 2024; https://www.eia.gov/todayinenergy/detail.php?id=65445, accessed May 20, 2025.

[4] Environmental; Institute, E. S. Fossil Fuels. 2024; https://www.eesi.org/topics/fossil-fuels/description, accessed May 21, 2025.

[5] U.S. Department of Energy, Office of Fossil Energy and Carbon Management Enhanced Oil Recovery. 2024; https://www.energy.gov/fecm/enhanced-oil-recovery, accessed May 17, 2025.

[6] Johns, R. T. In *Encyclopedia of Energy*; Cleveland, C. J., Ed.; Elsevier: New York, 2004; pp 701–713.

[7] Terry, R. E. In *Encyclopedia of Physical Science and Technology (Third Edition)*, third edition ed.; Meyers, R. A., Ed.; Academic Press: New York, 2003; pp 503–518.

[8] Collitt, S. D.; Sekhon, K. K.; Gomari, S. R.; Rahman, P. K. In *Challenges and Recent Advances in Sustainable Oil and Gas Recovery and Transportation*; Joshi, S., Jadhawar, P., Kumar, A., Eds.; Gulf Professional Publishing, 2023; pp 19–52.

[9] Kamal, M. S.; Sultan, A. S.; Al-Mubaiyedh, U. A.; and, I. A. H. Review on Polymer Flooding: Rheology, Adsorption, Stability, and Field Applications of Various Polymer Systems. *Polymer Reviews* **2015**, *55*, 491–530.

[10] Mohsenatabar Firozjaii, A.; Saghafi, H. R. Review on chemical enhanced oil recovery using polymer flooding: Fundamentals, experimental and numerical simulation. *Journal of Petroleum* **2020**, *6*, 115–122.

[11] Seright, R.; Wang, D. Polymer flooding: Current status and future directions. *Journal of Petroleum Science* **2023**, *20*, 910–921.

[12] Kaminsky, R. D.; Wattenbarger, R. C.; Szafranski, R. C.; Coutee, A. Guidelines for Polymer Flooding Evaluation and Development. Proceedings of the International Petroleum Technology Conference. 2007; pp IPTC–11200–MS.

[13] Oxford University Press A Dictionary of Mechanical Engineering. 2010; https://www.oxfordreference.com/display/10.1093/acref/9780199587438.001.0001/acref-9780199587438-e-7466, accessed June 26, 2025.

[14] Dhir, R. K.; Ghataora, G. S.; Lynn, C. J. In *Sustainable Construction Materials*; Dhir, R. K., Ghataora, G. S., Lynn, C. J., Eds.; Woodhead Publishing, 2017; pp 111–158.

[15] Liu, R.; Du, D.; Pu, W.; Peng, Q.; Tao, Z.; Pang, Y. Viscoelastic displacement and anomalously enhanced oil recovery of a novel star-like amphiphilic polyacrylamide. *Chemical Engineering Research and Design* **2019**, *142*, 369–385.

[16] Sandvik, E. I.; Maerker, J. M. *Extracellular Microbial Polysaccharides*; ACS Symposium Series; American Chemical Society, 1977; Vol. 45; Chapter 19, pp 242–264.

[17] Nadeau, P. H.; Sun, S.; Ehrenberg, S. N. The "Golden Zone" temperature distribution of oil and gas occurrence examined using a global empirical database. *Marine and Petroleum Geology* **2023**, *158*, 106507.

[18] Alnarabiji, M. S.; Husein, M. M. Application of bare nanoparticle-based nanofluids in enhanced oil recovery. *Fuel* **2020**, *267*, 117262.

[19] Hazarika, K.; Gogoi, S. B.; Kumar, A. Polymer flooding and its effects on enhanced oil recovery special reference to Upper Assam Basin. *Journal of Petroleum Research* **2023**, *8*, 54–62.

[20] Skauge, A.; Zamani, N.; Jacobsen, J.; Shaker Shiran, B.; Al-Shakry, B.; Skauge, T. Polymer Flow in Porous Media: Relevance to Enhanced Oil Recovery. *Colloids and Interfaces* **2018**, *2*, 27.

[21] Afsharpoor, A.; Balhoff, M. T.; Bonnecaze, R.; Huh, C. CFD modeling of the effect of polymer elasticity on residual oil saturation at the pore-scale. *Journal of Petroleum Science and Engineering* **2012**, *94-95*, 79–88.

[22] Zamani, N.; Bondino, I.; Kaufmann, R.; Skauge, A. Computation of polymer in-situ rheology using direct numerical simulation. *Journal of Petroleum Science and Engineering* **2017**, *159*, 92–102.

[23] Al-Shakry, B.; Skauge, T.; Shaker Shiran, B.; Skauge, A. *Impact of Mechanical Degradation on Polymer Injectivity in Porous Media*; National Library of Medicine, 2018; Vol. 10; p 742.

[24] Datta, S. S.; Ardekani, A. M.; Arratia, P. E.; Beris, A. N.; Bischofberger, I.; McKinley, G. H.; Eggers, J. G.; López-Aguilar, J. E.; Fielding, S. M.; Frishman, A.; Graham, M. D.; Guasto, J. S.; Haward, S. J.; Shen, A. Q.; Hormozi, S.; Morozov, A.; Poole, R. J.; Shankar, V.; Shaqfeh, E. S. G.; Stark, H.; Steinberg, V.; Subramanian, G.; Stone, H. A. Perspectives on viscoelastic flow instabilities and elastic turbulence. *Physical Review Fluids* **2022**, *7*, 080701.

[25] Steinberg, V. Elastic Turbulence: An Experimental View on Inertialess Random Flow. *Annual Review of Fluid Mechanics* **2021**, *53*, 27–58.

[26] Groisman, A.; Steinberg, V. Elastic turbulence in a polymer solution flow. *Nature* **2000**, *405*, 53–55.

[27] Clarke, A.; Howe, A. M.; Mitchell, J.; Staniland, J.; Hawkes, L.; Leeper, K. Mechanism of anomalously increased oil displacement with aqueous viscoelastic polymer solutions. *Soft Matter* **2015**, *11*, 3536–3541.

[28] Clarke, A.; Howe, A. M.; Mitchell, J.; Staniland, J.; Hawkes, L. A. How Viscoelastic-Polymer Flooding Enhances Displacement Efficiency. *Society of Petroleum Engineers Journal* **2016**, *21*, 0675–0687.

[29] Howe, A. M.; Clarke, A.; Giernalczyk, D. Flow of concentrated viscoelastic polymer solutions in porous media: effect of MW and concentration on elastic turbulence onset in various geometries. *Soft Matter* **2015**, *11*, 6419–6431.

[30] Mitchell, J.; Lyons, K.; Howe, A. M.; Clarke, A. Viscoelastic polymer flows and elastic turbulence in three-dimensional porous structures. *Soft Matter* **2016**, *12*, 460–468.

[31] Klemm, B.; Picchioni, F.; Raffa, P.; van Mastrigt, F. Star-Like Branched Polyacrylamides by RAFT polymerization, Part II: Performance Evaluation in Enhanced Oil Recovery (EOR). *Industrial & Engineering Chemistry Research* **2018**, *57*, 8835–8844, PMID: 30034090.

[32] Wever, D. A. Z.; Picchioni, F.; Broekhuis, A. A. Comblike Polyacrylamides as Flooding Agent in Enhanced Oil Recovery. *Industrial & Engineering Chemistry Research* **2013**, *52*, 16352–16363.

[33] Pu, W.-F.; Liu, R.; Wang, K.-Y.; Li, K.; Yan, Z.-P.; Li, B.; Zhao, L. Water-Soluble Core–Shell Hyperbranched Polymers for Enhanced Oil Recovery. *Industrial & Engineering Chemistry Research* **2015**, *54*, 798–807.

[34] Liu, R.; Pu, W.; Sheng, J. J.; Du, D. Star-like hydrophobically associative polyacrylamide for enhanced oil recovery: Comprehensive properties in harsh reservoir conditions. *Journal of the Taiwan Institute of Chemical Engineers* **2017**, *80*, 639–649.

[35] Castillo Sánchez, H. A.; Jovanović, M. R.; Kumar, S.; Morozov, A.; Shankar, V.; Subramanian, G.; Wilson, H. J. Understanding viscoelastic flow instabilities: Oldroyd-B and beyond. *Journal of Non-Newtonian Fluid Mechanics* **2022**, *302*, 104742.

[36] Hinch, J.; Harlen, O. Oldroyd B, and not A? *Journal of Non-Newtonian Fluid Mechanics* **2021**, *298*, 104668.

[37] Li, Z.; Wang, Y.; Alesadi, A.; Ruiz Pestana, L. A.; Xia, W. In *Fundamentals of Multiscale Modeling of Structural Materials*; Xia, W., Ruiz Pestana, L. A., Eds.; Elsevier, 2023; pp 75–111.

[38] Pakdel, P.; McKinley, G. H. Elastic Instability and Curved Streamlines. *Phys. Rev. Lett.* **1996**, *77*, 2459–2462.

[39] Groot, R. D.; Warren, P. B. Dissipative particle dynamics: Bridging the gap between atomistic and mesoscopic simulation. *The Journal of Chemical Physics* **1997**, *107*, 4423–4435.

[40] Kitanidis, P. K.; Dykaar, B. B. Stokes Flow in a Slowly Varying Two-Dimensional Periodic Pore. *Transport in Porous Media* **1997**, *26*, 89–98.

[41] Guazzelli, E.; Morris, J. F.; Pic, S. *A Physical Introduction to Suspension Dynamics*; Cambridge Texts in Applied Mathematics; Cambridge University Press, 2011.

[42] Winter, H. H. In *Modular Instruction Series C: Transport, Volume 7: Calculation and Measurement Techniques for Momentum, Energy and Mass Transfer*; Gordon, R. J., Ed.; American Institute of Chemical Engineers: New York, NY, 1987; Chapter C7.4, pp 27–34, AIChE Modular Instruction Series.

[43] Fedosov, D. A.; Pivkin, I. V.; Karniadakis, G. E. Velocity limit in DPD simulations of wall-bounded flows. *Journal of Computational Physics* **2008**, *227*, 2540–2559.

[44] Allen, M. P.; Tildesley, D. J. *Computer Simulation of Liquids*; Oxford University Press, 2017.

[45] Howard, M. P.; Truskett, T. M.; Nikoubashman, A. Cross-stream migration of a Brownian droplet in a polymer solution under Poiseuille flow. *Soft Matter* **2019**, *15*, 3168–3178.

[46] Español, P.; Warren, P. Statistical Mechanics of Dissipative Particle Dynamics. *Europhysics Letters* **1995**, *30*, 191.

[47] Fan, X.; Phan-Thien, N.; Chen, S.; Wu, X.; Yong Ng, T. Simulating flow of DNA suspension using dissipative particle dynamics. *Physics of Fluids* **2006**, *18*, 063102.

[48] Anderson, J. A.; Glaser, J.; Glotzer, S. C. HOOMD-blue: A Python package for high-performance molecular dynamics and hard particle Monte Carlo simulations. *Computational Materials Science* **2020**, *173*, 109363.

[49] Phillips, C. L.; Anderson, J. A.; Glotzer, S. C. Pseudo-random number generation for Brownian Dynamics and Dissipative Particle Dynamics simulations on GPU devices. *Journal of Computational Physics* **2011**, *230*, 7191–7201.

[50] https://github.com/mphowardlab/azplugins.

[51] Boerner, T. J.; Deems, S.; Furlani, T. R.; Knuth, S. L.; Towns, J. ACCESS: Advancing Innovation: NSF's Advanced Cyberinfrastructure Coordination Ecosystem: Services & Support. Practice and Experience in Advanced Research Computing (PEARC '23). New York, NY, USA, 2023; p 4.

[52] Revenga, M.; Zúñiga, I.; Español, P. Boundary conditions in dissipative particle dynamics. *Computer Physics Communications* **1999**, *121-122*, 309–311, Proceedings of the Europhysics Conference on Computational Physics CCP 1998.

[53] Pivkin, I. V.; Karniadakis, G. E. A new method to impose no-slip boundary conditions in dissipative particle dynamics. *Journal of Computational Physics* **2005**, *207*, 114–128.

[54] Pozrikidis, C. Creeping flow in two-dimensional channels. *Journal of Fluid Mechanics* **1987**, *180*, 495–514.

[55] Howard, M. P.; Nikoubashman, A.; Palmer, J. C. Modeling hydrodynamic interactions in soft materials with multiparticle collision dynamics. *Current Opinion in Chemical Engineering* **2019**, *23*, 34–43, Frontiers of Chemical Engineering: Molecular Modeling.